RESEARCH ARTICLE

METALLURGY

Atomic faulting induced exceptional cryogenic strain hardening in gradient cell–structured alloy

Qingsong Pan[1], Muxin Yang[2], Rui Feng[3], Andrew Chihpin Chuang[4], Ke An[3], Peter K. Liaw[5], Xiaolei Wu[2], Nairong Tao[1], Lei Lu[1]*

Coarse-grained materials are widely accepted to display the highest strain hardening and the best tensile ductility. We experimentally report an attractive strain hardening rate throughout the deformation stage at 77 kelvin in a stable single-phase alloy with gradient dislocation cells that even surpasses its coarse-grained counterparts. Contrary to conventional understanding, the exceptional strain hardening arises from a distinctive dynamic structural refinement mechanism facilitated by the emission and motion of massive multiorientational tiny stacking faults (planar defects), which are fundamentally distinct from the traditional linear dislocation–mediated deformation. The dominance of atomic-scale planar deformation faulting in plastic deformation introduces a different approach for strengthening and hardening metallic materials, offering promising properties and potential applications.

Strain hardening, also known as work hardening, which dates back to the Bronze Age, is the earliest widely used strategy to strengthen metallic materials (*1*). Traditionally, strain hardening results from a marked increase in the number of typical linear defects—i.e., dislocations—and their mutual interactions in crystalline lattice, which in turn tends to gradually reduce dislocation mobility (*2*–*6*). As a result, larger stresses are necessarily applied so that additional deformation may take place (*1*, *5*, *6*).

Generally, the soft coarse-grained (CG) metals display the highest strain hardening as well as the best tensile ductility because of the abundant space and the largest free path for movement and storage of dislocations (*4*, *7*). Dislocation-dislocation interactions in the crystalline solid give rise to local dislocation tangles and eventually a three-dimensional (3D) network of dislocation patterns (i.e., cell walls), where further deformation becomes difficult (*3*, *4*). In particular, the inherently thermal-assisted dislocation recovery and annihilation process gradually takes over to result in a gradually saturated substructural size at micrometer or submicrometer scale and a common drop in hardening rate with increasing strain (*1*, *4*, *7*).

The reduction in strain hardening becomes more pronounced in high-strength materials (*8*–*10*). Traditional strengthening methodologies—where strength is achieved either by changing composition or modifying hierarchical microstructures—are invariably built on the fundamental principle of blocking dislocation motion through incorporating various defects in a crystalline lattice, but they inevitably deteriorate strain hardening capacity (*1*, *10*–*16*). For example, nanostructured metallic materials containing massive grain boundaries (GBs) and heavily deformed materials containing a high density of dislocations have notably elevated strength yet exhibit markedly reduced strain hardening and limited uniform ductility down to a few percent (*8*, *9*). Strain hardening is essential because it effectively delocalizes flow strain, enhances tensile ductility, and inhibits catastrophic mechanical failure (*1*, *4*, *6*, *11*). However, substantial improvement in the strain hardening of high-strength metallic materials has been one of the thorniest problems of materials science over the past century.

Decreasing the deformation temperature substantially elevates strain hardening, essentially arising from the enhanced dislocation activity, such as reduced dynamic recovery and/or annihilation and the corresponding increased dislocation storage rate for various materials (*1*, *4*, *7*, *11*). When strain hardening is improved in this manner, deformation twinning and phase transformation may act as secondary carriers of crystal plasticity at low temperature (*17*–*20*). This scenario is particularly important for traditional single–principal element alloys with low stacking fault energies (SFEs) (*1*, *11*, *21*) and more recently developed high- to medium-entropy or multi–principal element (MPE) alloy systems (*22*–*30*). The presence of dynamic interactions between newly formed interfaces and dislocations contributes to a reasonable strain hardening capacity within a certain strain range. Essentially, dislocations are still acknowledged as the leading actor and dominate the plastic deformation of all metallic materials at cryogenic temperature (*1*, *4*, *11*, *31*).

Previous studies have shown that engineering spatially heterogeneous nanostructures containing gradient, bimodal grain sizes, multiphases, etc. could exhibit extra strain hardening compared with their homogeneous components because large plastic strain incompatibility induced an additional activity of geometry-necessary dislocations (*14*–*16*, *32*). However, the observed hardening as a result of strain gradients tends to be maintained only at the small plastic strain stage (<5%) and decreases at large strains, even at low temperature (*14*, *15*, *29*, *32*).

We recently discovered that cyclic torsion (CT)–induced ultrafine-scaled gradient dislocation cell structures (GDSs) in a single-phase $Al_{0.1}$CoCrFeNi MPE alloy activate massive parallel stacking faults (SFs) at ambient temperature, which are responsible for a high strength and considerable tensile plasticity (*33*). Inspired by this, we explored whether this GDS can effectively trigger SFs at low temperature to improve the strain hardening even at high strength.

Instead of developing parallel SFs, we observed extensive proliferation of multidirectional, extremely fine planar SFs starting from initial cell walls that induced a progressive structure refinement into tiny mosaic hierarchy. Along with the formation of traditional dislocations, the mosaic structure contributed to an exceptional strain hardening that even surpassed its CG counterparts at cryogenic temperature.

Gradient dislocation structure

The CG $Al_{0.1}$CoCrFeNi MPE alloy samples initially had randomly oriented grains with an average size of ~46 μm (fig. S1). We processed the dog bone–shaped bar MPE specimens (Fig. 1A) using CT treatment at ambient temperature to obtain a sample-level hierarchical GDS structure in the gauge section (4.5 mm in gauge diameter, 12 mm in gauge length) (Fig. 1B) [see (*33*) for processing details]. Both the grain size and morphology of the initial random-orientated grain structures were unchanged, having a homogeneous distribution from the surface to the core of the GDS sample (Fig. 1D). In particular, profuse low-angle boundaries, defined as those with a misorientation of <15°, were introduced in the grain interior and spatially distributed. The low-angle boundaries become lower in density with increasing depth from the top surface (Fig. 1E). We used transmission electron microscopy (TEM) observations to verify that abundant equiaxed dislocation cells, with a misorientation of ~2° on average, were pervasively formed in the topmost grains (~100 μm from the surface) (Fig. 1F). Each cell wall (~40-nm

[1]Shenyang National Laboratory for Materials Science, Institute of Metal Research, Chinese Academy of Sciences, Shenyang 110016, China. [2]State Key Laboratory of Nonlinear Mechanics, Institute of Mechanics, Chinese Academy of Sciences, Beijing 100190, China. [3]Neutron Scattering Division, Oak Ridge National Laboratory, Oak Ridge, TN 37831, USA. [4]Advanced Photon Source, Argonne National Laboratory, Lemont, IL 60439, USA. [5]Department of Materials Science and Engineering, The University of Tennessee, Knoxville, TN 37996, USA.
*Corresponding author. Email: llu@imr.ac.cn

thickness on average, corresponding to low-angle boundaries) had a high density of dislocations, which we verified using selected area diffraction patterning (Fig. 1F, inset). This feature separates the wall from the cell interior, which had low-density dislocations. We measured the cell diameter to be ~200 nm in the top surface that gradually increases to ~350 nm by 0.45-mm depth (Fig. 1, F and G).

By contrast, individual dislocations and related loose dislocation tangles are prevalently detected in grains at the core (Fig. 1H). We did not identify SFs or deformation twins, except for a few micrometer-spaced annealing twins (Fig. 1, E to H). The GDS sample is still in a state of a stable, single face-centered cubic (fcc) phase, as we show with our electron backscatter diffraction (EBSD) and TEM results (Fig. 1, D to H). This sample-level gradient dislocation architecture results in a distinct gradient distribution of microhardness (fig. S2)—gradually decreasing from 3.7 GPa at the topmost surface to 3.1 GPa at a 0.45-mm depth and 2.2 GPa in the central region of the as-prepared GDS sample, much larger than that of the dislocation-free CG (~1.7 GPa).

Strain hardening ability at 77 K

Both engineering (Fig. 2A) and true (Fig. 2B) stress-strain curves of quasistatic uniaxial tensile tests show that GDS samples have markedly elevated strength and ductility when reducing the temperature from 293 K to 77 K, similar to those of single-phase fcc metals and MPE alloy systems reported in the literature (*1*, *24*, *26*–*28*). Impressively, true yield strength (σ_y, at 0.2% offset) of the bulk GDS sample at 77 K is ~0.7 GPa, and its true ultimate tensile strength (σ_{UTS}) is more than 1.8 GPa, which is much higher than that of CG samples. In addition, a large strain hardening coefficient (i.e., true uniform elongation) is detected for the GDS alloy, ~0.48, slightly reduced relative to its CG counterpart (0.55) at 77 K (Fig. 2B).

Because the high density of dislocation cells is spatially concentrated in the surface layer of GDS samples, we removed the inner 3.6-mm-diameter core of GDS samples (Fig. 1C) to highlight the mechanical behavior of the high-density dislocation cell structure itself. Then, taken as an example, GDS tubular specimens with a sole surface architecture (~0.45-mm thickness) (hereafter referred to as the surface GDS) show a further enhanced strength at 77 K—i.e., true σ_y and σ_{UTS} up to ~0.9 GPa and 2.4 GPa, respectively, and a considerable true uniform elongation as large as ~50%, comparable to that of the bulk GDS and CG counterpart (Fig. 2B).

Analysis of tensile test results for the CG yields a monotonically decreased strain hardening rate (Θ) upon straining more than 1% at both 293 K and 77 K (Fig. 2C). Obviously, the strain hardening rates of both the GDS and surface GDS samples at 293 K are still lower than that of CG sample owing to the presence of numerous preexisting dislocations, consistent with the literature data (*9*, *14*, *27*, *28*). By contrast, we observed an unexpectedly high Θ in the GDS at 77 K, even higher than that of its CG counterpart, throughout the entire plastic deformation stage. Notably, the strain hardening rate of the surface GDS becomes further elevated—i.e., with Θ gradually decreased from 4.2 GPa at a 3% strain to 2.4 GPa before necking—compared with CG (from 3.1 to 1.6 GPa) and GDS specimens (Fig. 2C).

We observed the same trend in the strain hardening rate normalized by flow stress (Θ/σ) versus true stress (Fig. 2D), showing a higher Θ/σ in GDS and the highest Θ/σ in surface GDS compared with that of CG at 77 K. The notably superior strain hardening behavior agrees well with the remarkable microhardness increment at the topmost GDS layer from the initial 3.7 GPa to 5.0 GPa after a 40% strain—the latter is much higher than that for the GDS core and CG counterparts (~4.1 GPa) at 77 K (fig. S2). Such ultrahigh strain hardening rate and ductility in GDS samples are rarely seen in conventional high-strength metallic materials and MPE alloys with dislocation-dominated strain hardening (*1*, *11*, *28*), and they indicate the presence of an unusual strain hardening mechanism inherent to gradient dislocation structures upon straining at 77 K.

To demonstrate the excellent strength-strain hardening synergy of GDS samples at 77 K, we compare their uniform elongation versus ultimate tensile strength (Fig. 2E) with those of the same compositions with homogeneous and gradient-grained structures at 293 K and 77 K (*34*–*36*) and with other MPE alloy systems (*37*–*42*) as well as the advanced cryogenic steels (*21*, *43*, *44*) at 4.2 K to 77 K, which correspond to various strengthening strategies. We normalized the strength by the Young's modulus of the material. A superb ductile and strong GDS at 77 K stands out from the general mechanical trade-off performance of other materials—i.e.,

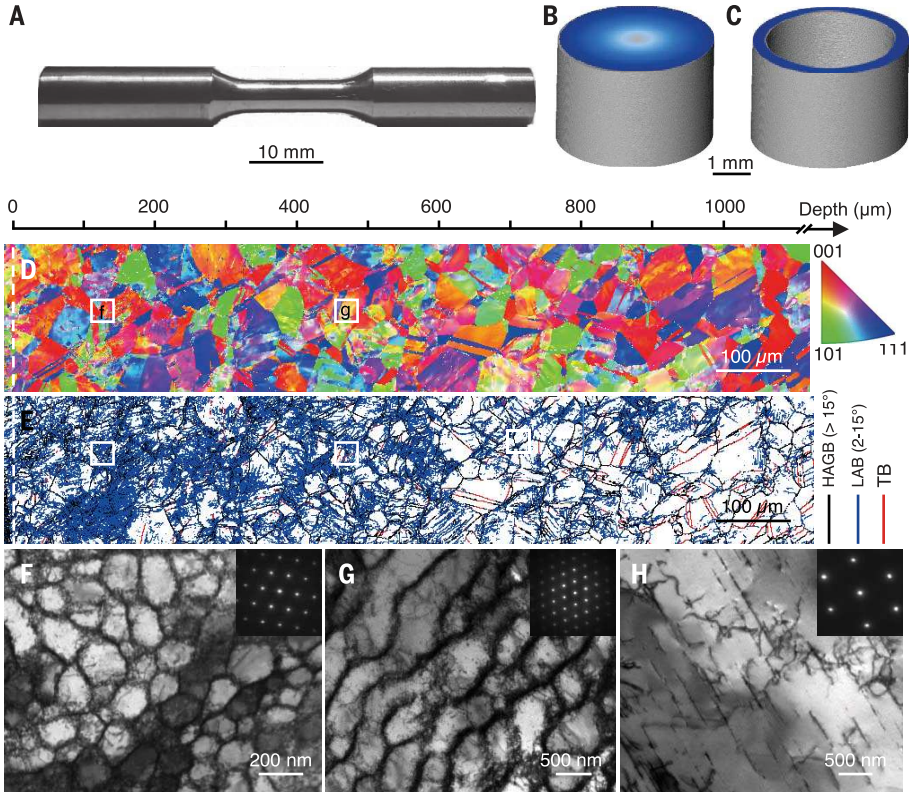

Fig. 1. Typical microstructure of GDS alloy. (**A**) The image of the dog bone–shaped GDS bar sample, of which the gauge section was processed by means of CT processing. (**B**) Cross-sectional schematic showing a sample-level GDS structure from surface (dark blue) to core (light gray). (**C**) 3D x-ray tomographic reconstruction of the gauge section of a GDS tubular sample (~0.45-mm thickness). (**D** and **E**) Cross-sectional EBSD images of the GDS alloy showing the distributions of grain-scaled morphology, orientation (D), and three types of boundaries defined with different misorientation angles (E) within a depth of 1.0 mm from the surface. HAGB, high-angle grain boundary; LAB, low-angle boundary. (**F** to **H**) The bright-field TEM images [(F) and (G)] at the positions of the white squares in (D) and that at the core (H), showing a hierarchical GDS structure. The insets in (F) to (H) are the corresponding selected area electron diffraction (SAED) patterns.

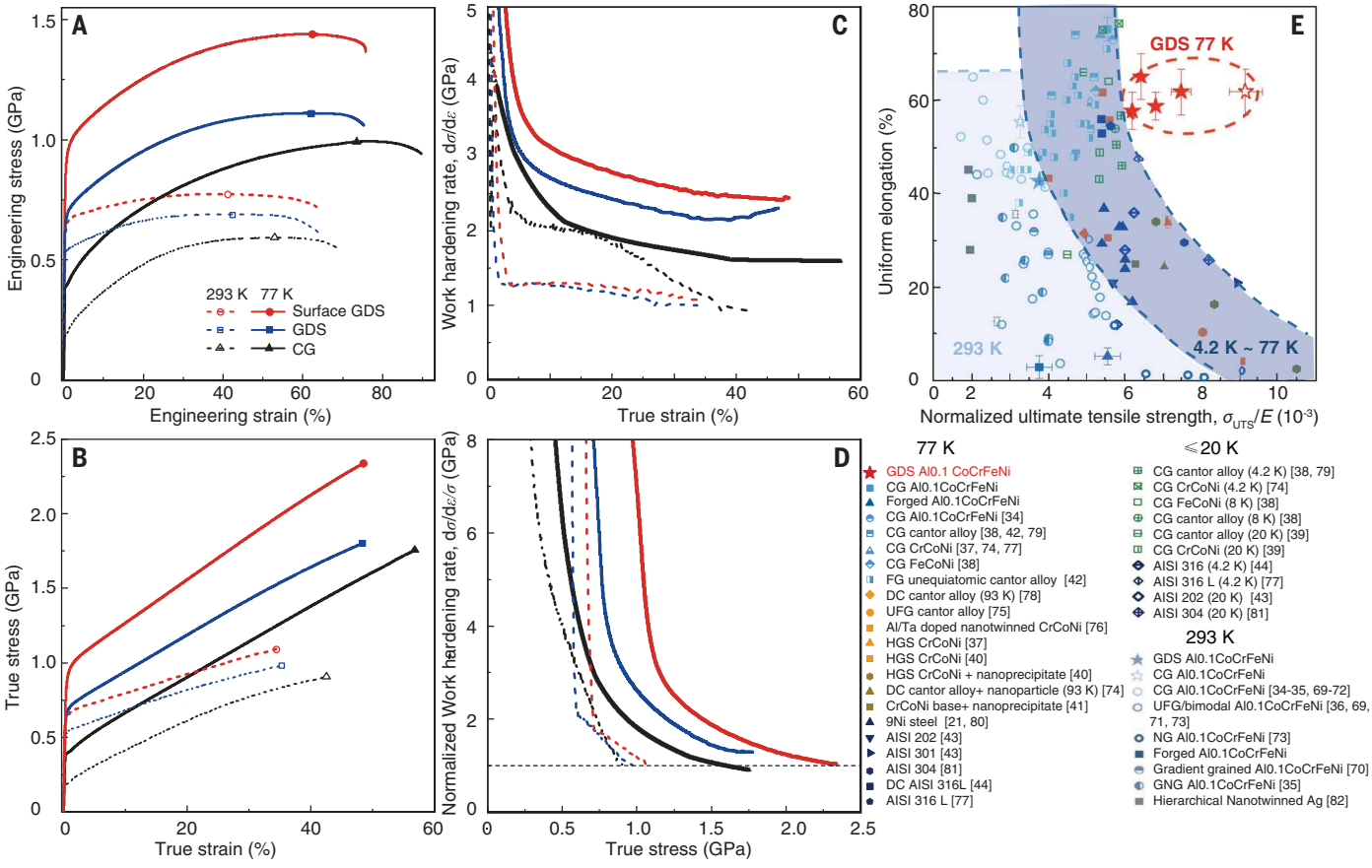

Fig. 2. Strain hardening and strength-ductility combination of GDS alloy at 77 K. (**A** and **B**) Tensile engineering (A) and true (B) stress-strain curves of GDS, surface GDS, and CG samples at 293 K and 77 K. (**C** and **D**) The corresponding strain hardening rate and true strain relations (C) and normalized strain hardening rate by flow stress and true stress relations (D). (**E**) Strength and ductility synergy of GDS alloy, compared with other high-performing materials at cryogenic temperature. Uniform elongation versus ultimate tensile strength normalized by Young's modulus of the GDS alloy, compared with those of the same compositions (with homogeneous, gradient-grained structures) at 293 K and 77 K (*34*–*36*), other MPE alloys (*37*–*42*), and cryogenic steels (*21*, *43*, *44*) tensioned from 4.2 K to 77 K in the literature. The hollow five-pointed star denotes the property of the topmost GDS surface with the use of the strength value estimated from the *Hv*/3 and uniform elongation data from tensile test of GDS layer. The error bars represent standard deviations from more than three independent tensile tests. DC, dislocation cell; UFG, ultrafine grain; HGS, heterogeneous grain structure; FG, fine grain; NG, nanograin.

the overall strength gain usually comes at the expense of a severe ductility loss (Fig. 2E).

Dynamic stacking faulted (SFed) mosaics induced strain hardening mechanism

Focusing on deciphering the underlying unusual strain hardening mechanism of GDS at cryogenic temperature, we further characterized the microstructures at the top surface of GDS by interrupting tensile tests at the early stage (3%) (Fig. 3, A to C, and fig. S3) and the later stage of plasticity (40%) (Fig. 3, D to G, and fig. S4) at 77 K. At the strain of 3%, the dislocation cells remain almost unchanged in shape and size. Specifically, plentiful events of different orientated lamellar bundles intersecting with each other were identified inside the grains, independent of grain orientations (denoted by dashed lines in Fig. 3, A and B, and fig. S3), which was rarely detected in the surface of the GDS tensile deformed at 293 K (*33*). Atomic-resolution, aberration-corrected high-angle annular dark-field scanning transmission electron microscopy (HAADF-STEM) views further revealed that these interlocked lamellae are multiple SF bundles and twin boundary (TB) segments in different (111) slip planes, with an average value of 22 nm in length (Fig. 3C). The statistic of the thickness between neighboring SFs or TBs is only 2.8 nm on average, corresponding to a high density of defects (~1.3×10^{17} m^{-2}) in the lamellar bundles.

At tensile strain up to 40%, the mutually intersected planar interfaces notably proliferate, further subdividing the microsized topmost surface grains into nanometer-sized mosaics (Fig. 3, D to F). The initial equiaxed dislocation cells and walls in these grains have disappeared; instead, abundant mosaic-shaped substructures prevail in the grain interior (Fig. 3F), with a mean size of ~50 nm. Our HAADF images identify more details indicating that these mosaics are further refined by individual tiny mosaics, which contain extremely fine SFs and twins and are separated primarily by low-angle misorientation (<15°) (Fig. 3G). We named these structures tiny SFed mosaics. The spacing between adjacent SFs or TBs in tiny SFed mosaics is ~1.8 nm, whereas their length is ~20 nm on average.

The presence of ultrafine SFs and TBs at 77 K indicates an extremely high density of planar interfacial defects, ~3.1×10^{17} m^{-2}, which is about six times as high as that (~5.2×10^{16} m^{-2}) in GDS deformed at 293 K (*33*). By contrast, intensive dislocations along primarily slip planes, with a small quantity of parallel SFs and deformation twins, dominate the plastic strain of CG at 77 K (fig. S5) and the core of bulk GDS samples at 77 K, similar to most single fcc MPE alloys with low SFEs at low temperature (*27*, *28*, *45*, *46*).

Quantitative composition analysis at the nanometer scale by means of energy-dispersive x-ray spectroscopy mapping displays a homogeneous distribution for each element without

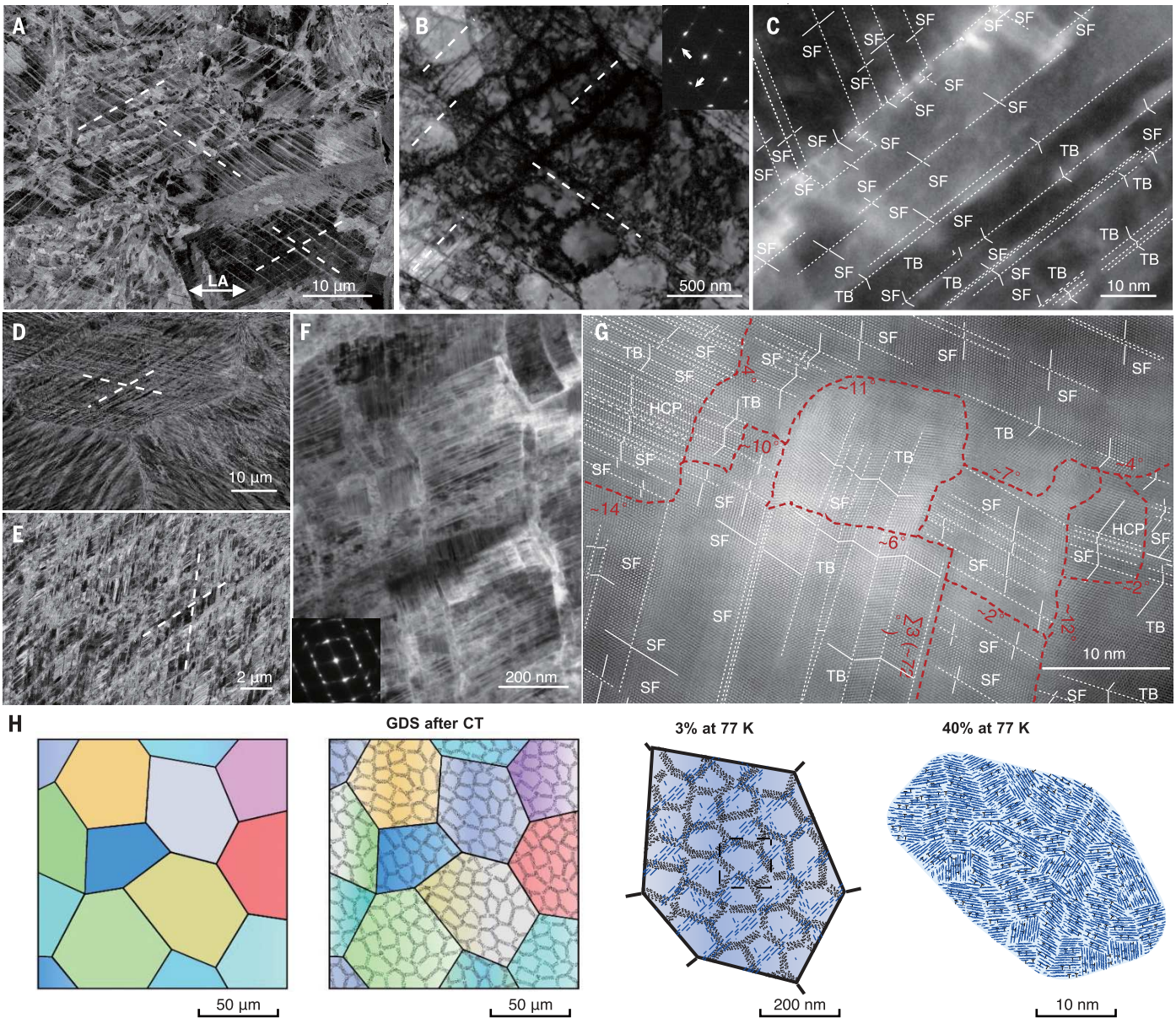

Fig. 3. Microstructural evolution of the GDS surface layer during tension at 77 K. (**A** and **B**) The cross-sectional SEM (A) and bright-field TEM (B) images of the GDS surface layer at 3% tensile strain, showing the widespread occurrence of two sets of SF bundles (indicated by the white arrows) at different {111} slip planes and across multiple dislocation cell patterns in the topmost surface. The white line with double arrows in (A) denotes the loading axis (LA). The corresponding SAED patterns in (B) contain two sets of parallel streaks from SFs (along two [111] directions, noted by the white arrows). (**C**) An aberration-corrected HAADF-STEM image taken from one SF bundle, revealing an ultrahigh density of SFs and TBs. (**D** and **E**) The cross-sectional SEM images of the GDS surface layer at 40% tensile strain, showing an example of one grain containing denser mutually inclined planar interfaces (denoted as white dashed lines). (**F**) HAADF-STEM image showing massive nanomosaics in the one grain interior. The inset at the bottom left is the corresponding SAED pattern. (**G**) Atomic-resolution HAADF-STEM image showing a typical example of several tiny mosaics of ~10-nm scale in size (sketched as red dashed curves) containing atomic-scaled SFs at different {111} slip planes. The numbers in red denote the misorientation angles of the interfaces separating the adjacent SFed mosaics. (**H**) Schematic illustration showing the dynamic structural refinement process of initial dislocation cell structure enabled by the formation of extensive nanomosaics during the tensile experiment at 77 K.

any detectable compositional segregation in SFed mosaics (fig. S4). This is analogous to that in the as-prepared state (*33*), possibly owing to the suppressed atomic diffusion of elements when performing the tensile tests in liquid nitrogen.

Synchrotron x-ray diffraction (SXRD) scans from the topmost surface to the core of both GDS and CG samples after tension showed higher SF and twin probabilities at 77 K compared with those at 293 K at the same strains (Fig. 4A and fig. S6), which verifies the readier formation of SFs and twins at 77 K, as previously reported in other studies (*24*, *26*, *39*, *45*–*47*). Notably, we obtained a higher value of the SFs and twins probability in the surface GDS layer at 3% at 77 K, even higher than those of CG tension loaded at a strain of 40% at 293 K. With increasing the tension strain (40%) at 77 K, the further-elevated SF and twin probability is evidently detected in the surface GDS layer compared with CG and the core of GDS sample, which is fully consistent with our ex situ SEM and TEM observations (Fig. 3). Such

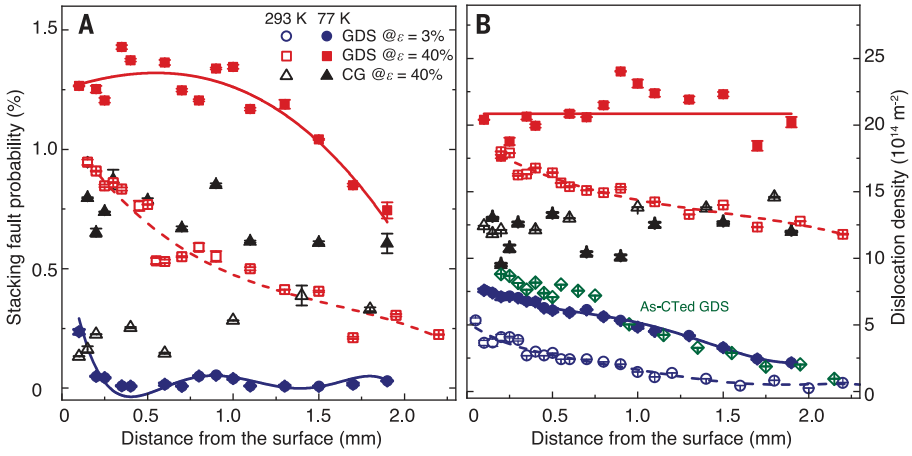

Fig. 4. The evolution of SF probability and dislocation density in the GDS and CG alloys after tension at 77 K. (**A** and **B**) The evolution of SF probability (A) and full dislocation density (B) from the topmost surface to the core of GDS and CG (tensile strained 3% and 40%) samples at 293 K and 77 K, determined by the extended convolutional multiple whole profile (eCMWP) fitting analysis on SXRD spectrums. SF probabilities in the 3% deformed GDS sample at 293 K were too low to be extracted.

an elevated SF and twin probability is also expected in the surface GDS samples because they have the same GDS structure (i.e., size and distribution of dislocation cells) as bulk GDS samples.

The extended convolutional multiple whole-SXRD profile analysis also reveals a much higher density of dislocation density in the GDS samples at 77 K (up to 2.0×10^{15} m^{-2} at a 40% tensile strain) compared with those in the GDS at 293 K and the CG counterparts at 77 K (Fig. 4B). In addition, the SXRD profiles from the topmost surface to the core of GDS after tensile deformation still display a stable single fcc phase without detectable peaks from any hcp phases (fig. S6), also resembling the microstructure displayed in Fig. 3.

Traditional strengthening mechanisms invariably confront a thorny dilemma: They strongly resist dislocations yet greatly reduce their accumulation density in fine structures (diminished strain hardening), even at cryogenic temperature (*11*, *13*, *28*, *29*), as we also explicitly demonstrated in Fig. 2E. By contrast, on the basis of our results, we rationalize that through engineering metastable ultrafine dislocation cells, a mechanism of massive multiorientational tiny planar SFs mediated dynamic structural refinement, effectively blocks and accumulates dislocations simultaneously, and is responsible for an exceptionally high strain hardening rate at 77 K.

Linear dislocations are the primary and easiest elementary strain carrier in crystalline materials (*1*, *11*). The strain hardening of polycrystalline metals is essentially attributed to the motion, mutual obstruction, and accumulation of dislocations on multiple slip systems and their progressive self-organization into saturated dislocation patterns aided by intrinsic high-dynamic recovery of dislocations (*4*, *11*, *48*). Without exception, intensive multiple dislocations glide and interact, subsequently resulting in the formation of submicrometer-sized dislocation cells and walls, having a very high density of dislocations, as we observed in the as-prepared GDS sample during the CT process (Fig. 1 and Fig. 3H). However, contradictory to the conventional wisdom of less potential for further storing dislocation in high-strength metals with high density of preexisting interfaces or dislocations (*1*, *10*, *11*), atomic-scale multiple-slip SFed mosaics, besides high-density dislocations, are robustly triggered in highly dislocated GDS after tension at 77 K. Previous studies have reported that the introduction of nanoprecipitates in MPE alloys facilitates multiple SF slips at 77 K (*41*, *49*). However, this trend only occurs in a very locally large stress-strain regime, mostly adjacent to the nanoprecipitates with a limited volume fraction.

The nucleation of profuse multiple SFs initially arises from the emission process from numerous cell walls of GDS, which contain an ultrahigh dislocation density—i.e., acting as the abundant preexisting intragrain sources owing to the intrinsic locally varied, low-SFE feature of the MPE alloy containing saliently rugged local concentration fluctuations [6 to 21 mJ/m^2 at room temperature (*50*)]. In particular, similar to most fcc MPE alloys at low temperature (*26*, *28*, *39*, *45*–*47*), the SFE of material is monotonically reduced at 77 K, which further increases the tendency of activation and expansion of multiple SFs. In addition, because it is structural size dependent (*51*, *52*), deformation planar faulting, compared with the classic linear dislocation activity, is more favorable in ultrafine-sized dislocation cells at 77 K. The intrinsic reason for the formation of SFs has been discussed in detail by Pan *et al.* (*33*). Under such optimal thermodynamical circumstances, the ready, multiple-glide feature of abundant mobile SFs makes them the potentially dominant carrier to mediate plastic strains, analogous to the traditional dislocations.

Upon tensile strain, the built-in progressive gradient plastic deformation feature in GDS substantially enables strain delocalization and allows for the dominance of abundant multiple SF activation to mediate both statistically stored and geometrically necessary plastic strain in conjunction with dislocations (*14*–*16*, *53*, *54*). A strong locally complex multiaxial stress field coupled with gradient straining and strain path effect from torsion to tension may be built in at 77 K, providing a markedly high internal driving force for the activation and gliding of more multiple SFs (*4*, *55*), as reasonably evidenced by the ultrahigh microhardness in surface GDS and orientation-independent character of the numerous topmost grains containing SFs at 77 K (figs. S2 and S3).

A SF has a salient 2D stable planar feature, different from the flexible line defect of dislocations (*3*). As such, with increasing imposed stress, a greater number of multiple 2D SF interfaces readily propagate from cell walls and interact with each other at various slip planes, progressively subdividing the initial dislocation walls into parallel SF bundles (Fig. 3, A to C and H). Subsequently, the newly formed massive SFs and their intensive interactions with cell walls, and/or individual dislocation also act as additional, dynamically formed, and sustainable sources that accelerate the storage rate of planar SFs and linear dislocations therein via long-range stress (fig. S7). Besides SFs, we also detected more planar TBs at higher tensile strain, yet far fewer than the number of SFs (Fig. 3), primarily resulting from the by-product of the continuous SFs glide with the same sign on consecutive {111} atomic planes from cell walls or their interactions with dislocations (*1*, *17*, *56*).

Specially, the 2D SF interface tends to become more stable at 77 K, corresponding to a less–thermally assisted annihilation process during tensile straining compared with linear dislocation. Taken together, as a result of superhigh-density SF and TB accumulation, continuous net SF and TB pump naturally causes progressive in situ structural refinement from submicrometer-sized cell walls into more tiny SFed mosaics, containing extremely fine SFs and TBs as well as a high density of dislocations (Fig. 3, D to H, and Fig. 4B).

The prominent structural feature of SFed mosaics is that they contain a high density of multiple, short, yet thin SFs and TBs. These come from the synergistic combination effects of the GDS structure and the rugged local concentration fluctuation environments of MPE alloys that occur intrinsically as well as the cryogenic temperature condition. Due to the lowest energy of these basic deformation structural

units of SFs and TBs, the deformation-induced transition from metastable dislocation cells to further refined tiny SFed mosaics is thus considered to be an autonomous structural evolution process close to the minimum free energy, strictly obeying the classic strain hardening principles of metals—i.e., self-organizations and low-energy structures (*4*, *48*).

As demonstrated by experiments and molecular dynamic simulations (*56*, *57*), nanometer-spaced SF interfaces are able to hinder dislocation motion as effectively as nanoscale TBs and GBs. Therefore, the dynamic structural refinement process from the initial cells to finer SFed mosaics built-in grain interiors plays dual roles—not only effectively accumulating dislocations but also hindering them simultaneously, greatly increasing slip resistance. This process, together with intensive dislocation-dislocation interaction–induced pronounced forest strengthening, dynamically hardens the GDS surface layer much faster and substantially higher than the bulk GDS and CG at 77 K throughout the tensile test (Fig. 2B).

By conducting the tensile load-unload-reload tests (*1*, *14*, *15*, *37*), as shown in fig. S7, we observed that both back stress and effective stress, partitioning from the true flow stress, monotonically increase with increasing tensile strain for GDS at 77 K and are higher than that of the CG counterpart through the entire uniform straining range. In particular, the increase in the internal back stresses (up to 1.4 GPa before necking) is the decisive contributor to the flow stress of bulk GDS after yielding, accounting for ~70% of the total flow stress during strain hardening. The enhanced long-range back stress hardening arises from initial ultrafine dislocation cells and later dynamic generation of tiny mosaics, whereas the high short-range effective stress originates from forest dislocation hardening of higher-density dislocations. Coupled high back stress and effective stress are collectively responsible for the excellent strain hardening of GDS throughout tensile straining at cryogenic temperature (Fig. 2, C and D). As such, the sustainable, high-strain hardening rate consequently enables GDS samples a high ductility (or strain hardening coefficient) at gigapascal flow stresses after yielding at ~0.9 GPa (Fig. 2B).

Our experimental observations point to an unusual strain hardening mechanism that is readily triggered by the formation of extremely refined SFed mosaics in a single fcc phase MPE alloy with gradient dislocation structure at cryogenic temperature, giving it an unprecedentedly high strain hardening capacity, even beyond that of its CG counterpart. This dynamic SFed mosaics–induced strain hardening mechanism at cryogenic temperature echoes our earlier results of SF-induced plasticity as well as the exceptional strength and ductility in the GDS alloy at room temperature (*33*, *58*). Evidently, the underlying dominant atomic-scale planar deformation faulting activities in crystalline lattice not only play an alternative, elementary carrier of crystal plasticity but also induce robust strain hardening compared with the linear dislocations. The feature of gradient dislocation architectures and nanosized SFs mosaics is of great importance for understanding the fundamental strain hardening mechanism from physical metallurgy and provides a different paradigm for developing strong and ductile materials, especially for a wide spectrum of cryogenic applications, such as deep space and ocean exploration, liquefied natural gas storage, cryogenic physics, and so on.

REFERENCES AND NOTES

1. M. A. Meyers, K. K. Chawla, *Mechanical Behavior of Materials* (Cambridge Univ. Press, ed. 2, 2009).
2. G. I. Taylor, *Proc. R. Soc. Lond. A* **145**, 362–387 (1934).
3. J. P. Hirth, J. Lothe, *Theory of Dislocations* (Wiley, ed. 2, 1982).
4. F. R. N. Nabarro, M. S. Duesbery, *Dislocations in Solids* (Elsevier, 2002).
5. B. Devincre, T. Hoc, L. Kubin, *Science* **320**, 1745–1748 (2008).
6. L. A. Zepeda-Ruiz *et al*., *Nat. Mater.* **20**, 315–320 (2021).
7. U. F. Kocks, H. Mecking, *Prog. Mater. Sci.* **48**, 171–273 (2003).
8. T. H. Fang, W. L. Li, N. R. Tao, K. Lu, *Science* **331**, 1587–1590 (2011).
9. M. A. Meyers, A. Mishra, D. J. Benson, *Prog. Mater. Sci.* **51**, 427–556 (2006).
10. K. Lu, *Nat. Rev. Mater.* **1**, 16019 (2016).
11. A. S. Argon, *Strengthening Mechanisms in Crystal Plasticity* (Oxford Univ. Press, 2008).
12. T. Zhu, J. Li, *Prog. Mater. Sci.* **55**, 710–757 (2010).
13. K. Lu, L. Lu, S. Suresh, *Science* **324**, 349–352 (2009).
14. X. Wu, P. Jiang, L. Chen, F. Yuan, Y. T. T. Zhu, *Proc. Natl. Acad. Sci. U.S.A.* **111**, 7197–7201 (2014).
15. X. Y. Li, L. Lu, J. G. Li, X. Zhang, H. J. Gao, *Nat. Rev. Mater.* **5**, 706–723 (2020).
16. Y. T. Zhu *et al*., *Mater. Res. Lett.* **9**, 1–31 (2020).
17. J. W. Christian, S. Mahajan, *Prog. Mater. Sci.* **39**, 1–157 (1995).
18. B. C. De Cooman, Y. Estrin, S. K. Kim, *Acta Mater.* **142**, 283–362 (2018).
19. D. A. Porter, K. E. Easterling, M. Y. Sherif, *Phase Transformations in Metals and Alloys* (CRC Press, ed. 4, 2021).
20. M. Soleimani, A. Kalhor, H. Mirzadeh, *Mater. Sci. Eng. A* **795**, 140023 (2020).
21. C. R. Anoop *et al*., *Mater. Perform. Charact.* **10**, 20200193 (2021).
22. B. Cantor, I. T. H. Chang, P. Knight, A. J. B. Vincent, *Mater. Sci. Eng. A* **375–377**, 213–218 (2004).
23. J. W. Yeh *et al*., *Adv. Eng. Mater.* **6**, 299–303 (2004).
24. B. Gludovatz *et al*., *Science* **345**, 1153–1158 (2014).
25. Z. Li, K. G. Pradeep, Y. Deng, D. Raabe, C. C. Tasan, *Nature* **534**, 227–230 (2016).
26. F. Otto *et al*., *Acta Mater.* **61**, 5743–5755 (2013).
27. E. P. George, W. A. Curtin, C. C. Tasan, *Acta Mater.* **188**, 435–474 (2020).
28. W. Li *et al*., *Prog. Mater. Sci.* **118**, 100777 (2021).
29. P. Sathiyamoorthi, H. S. Kim, *Prog. Mater. Sci.* **123**, 100709 (2022).
30. E. P. George, D. Raabe, R. O. Ritchie, *Nat. Rev. Mater.* **4**, 515–534 (2019).
31. E. Ma, *Scr. Mater.* **181**, 127–133 (2020).
32. Z. Cheng, H. Zhou, Q. Lu, H. Gao, L. Lu, *Science* **362**, eaau1925 (2018).
33. Q. Pan *et al*., *Science* **374**, 984–989 (2021).
34. Z. Lyu *et al*., *J. Mater. Res.* **33**, 2998–3010 (2018).
35. G. Chen *et al*., *Scr. Mater.* **167**, 95–100 (2019).
36. S. Gangireddy, L. Kaimiao, B. Gwalani, R. Mishra, *Mater. Sci. Eng. A* **727**, 148–159 (2018).
37. M. Yang *et al*., *Proc. Natl. Acad. Sci. U.S.A.* **115**, 7224–7229 (2018).
38. A. S. Tirunilai *et al*., *Mater. Sci. Eng. A* **783**, 139290 (2020).
39. D. Liu *et al*., *Science* **378**, 978–983 (2022).
40. Z. Zhang *et al*., *J. Mater. Res. Technol.* **17**, 3262–3276 (2022).
41. D. Ma, H. Xu, J. Ding, Y. Shen, T. Zhang, *Mater. Sci. Eng. A* **862**, 144489 (2023).
42. C. Wagner, G. Laplanche, *Acta Mater.* **244**, 118541 (2023).
43. C. J. Guntner, R. P. Reed, in *Advances in Cryogenic Engineering*, K. D. Timmerhaus, Ed. (Springer, 1961), pp. 565–576.
44. R. Bidulský *et al*., *Materials* **13**, 3328 (2020).
45. J. Moon *et al*., *Mater. Today* **50**, 55–68 (2021).
46. M. Naeem *et al*., *Sci. Adv.* **6**, eaax4002 (2020).
47. Q. Ding *et al*., *Nature* **574**, 223–227 (2019).
48. D. Kuhlmann-Wilsdorf, *Metall. Mater. Trans. A* **35**, 369–418 (2004).
49. Y. Tong *et al*., *Acta Mater.* **165**, 228–240 (2019).
50. X. D. Xu *et al*., *Acta Mater.* **144**, 107–115 (2018).
51. E. Orowan, in *Symposium on Internal Stresses in Metals and Alloys* (Institute of Metals, 1948).
52. R. J. Asaro, P. Krysl, B. Kad, *Philos. Mag. Lett.* **83**, 733–743 (2003).
53. M. F. Ashby, *Philos. Mag.* **21**, 399–424 (1970).
54. N. A. Fleck, M. F. Ashby, J. W. Hutchinson, *Scr. Mater.* **48**, 179–183 (2003).
55. H. Mughrabi, *Acta Metall.* **31**, 1367–1379 (1983).
56. R. Z. Su *et al*., *Mater. Sci. Eng. A* **803**, 140696 (2021).
57. X. Feng *et al*., *Nanoscale* **10**, 13329–13334 (2018).
58. J. W. Yeh, *Science* **374**, 940–941 (2021).

ACKNOWLEDGMENTS

We thank X. W. Huang for performing HAADF-STEM experiments, S. G. Wang for performing x-ray tomography experiments and analyzing the results, C. H. Li for performing EBSD experiments, and N. Lu and J. Xu for analyzing TEM and EBSD results. **Funding:** Q.P. and L.L. acknowledge financial support by the National Science Foundation of China (NSFC) (grant nos. 51931010, 92163202, 52122104, and 52071321), the Key Research Program of Frontier Science and International partnership program (GJHZ2029), and the Youth Innovation Promotion Association (2019196) of the Chinese Academy of Sciences (CAS). P.K.L. acknowledges support from the National Science Foundation (DMR-1611180, 1809640, and 2226508) and the US Army Research Office (W911NF-13-1-0438 and W911NF-19-2-0049). R.F. acknowledges support from the Material Engineering Initiative (MEI) at the Spallation Neutron Source (SNS), Oak Ridge National Laboratory. M.Y. acknowledges support from NSFC (52071326). SXRD experiments were conducted at the Advanced Photon Source (APS), a US Department of Energy (DOE) Office of Science User Facility operated for the DOE Office of Science by the Argonne National Laboratory under contract no. DE-AC02-06CH11357. This research used resources at the SNS, a DOE Office of Science User Facility operated by the Oak Ridge National Laboratory. **Author contributions:** L.L. initiated and supervised the project. Q.P. and M.Y. prepared the samples and performed the experiments. A.C.C., K.A., and R.F. guided and performed the SXRD experiments and results. R.F. carried out the diffraction line profile analysis. Q.P. and L.L. designed the experiments and drafted the manuscript. All the coauthors contributed to the discussions and revised the manuscript. **Completing interests:** The authors declare no competing interests. **Data and materials availability:** All data generated or analyzed during this study are included in this published article and its supplementary materials.

SUPPLEMENTARY MATERIALS

science.org/doi/10.1126/science.adj3974
Materials and Methods
Supplementary Text
Figs. S1 to S7
References (*59*–*82*)

Submitted 24 June 2023; accepted 1 September 2023
Published online 14 September 2023
10.1126/science.adj3974